Journal of Physics D: Applied Physics

PAPER

# Synthetically encapsulated & self-organized transition metal oxide nano-structures inside carbon nanotubes as robust: Li-ion battery anode materials

To cite this article: Aakanksha Kapoor *et al* 2023 *J. Phys. D: Appl. Phys.* **56** 425504

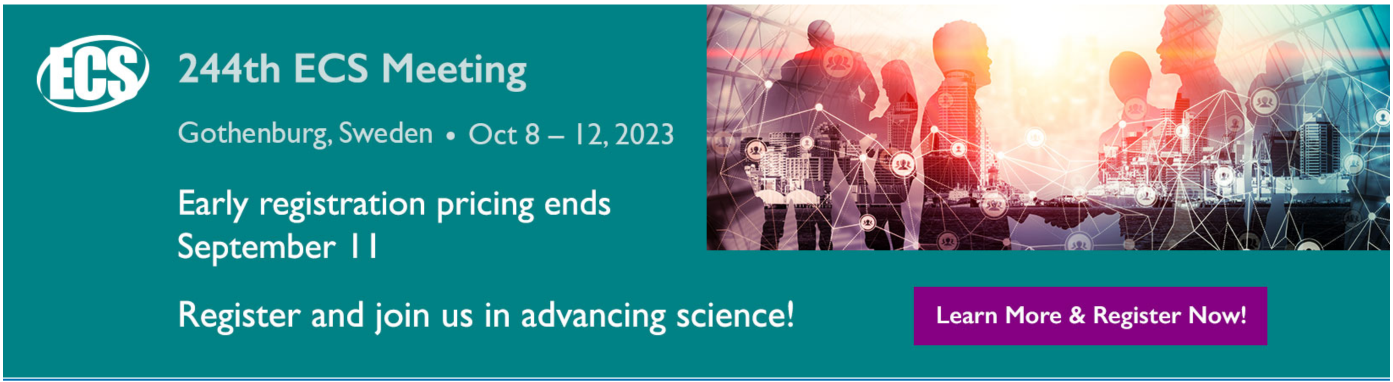

**IOP** Publishing
Journal of Physics D: Applied Physics
J. Phys. D: Appl. Phys. **56** (2023) 425504 (10pp)
https://doi.org/10.1088/1361-6463/ace3d7

# Synthetically encapsulated & self-organized transition metal oxide nano-structures inside carbon nanotubes as robust: Li-ion battery anode materials

**Aakanksha Kapoor[1,2], Apurva L Patrike[1], Nitesh Singh[1], Elisa Thauer[3], Alexander Ottmann[3], Rüdiger Klingeler[3,4], Satishchandra Ogale[1,5] and Ashna Bajpai[1,6,*]**

[1] Department of Physics, Indian Institute of Science Education and Research, Dr Homi Bhabha Road, Pune 411008, India
[2] Department of Physics, SRM University, Sonepat, Delhi NCR, India
[3] Kirchhoff Institute of Physics, Heidelberg University, D-69120 Heidelberg, Germany
[4] Centre for Advanced Materials (CAM), Heidelberg University, D-69120 Heidelberg, Germany
[5] Research Institute for Sustainable Energy (RISE), TCG-Centres for Research and Education in Science and Technology, Sector V, Salt Lake, Kolkata 700091, India
[6] Centre for Energy Science, Indian Institute of Science Education and Research, Pune 411008, India

E-mail: ashna@iiserpune.ac.in

Received 23 February 2023, revised 21 June 2023
Accepted for publication 4 July 2023
Published 26 July 2023

## Abstract

We report a comparative study on the electrochemical performance of four different transition metal oxides encapsulated inside carbon nanotubes (oxides@CNT), along with reference data obtained on a *bare-oxide*. A key result here is that the encapsulation leads to superior *cyclic stability*, irrespective of the type of the oxide-encapsulate. This comparison also enables us to isolate the advantages associated with the encapsulation of oxide within the core cavity of CNT, as opposed to the case of oxide/CNT composites, in which oxide resides outside the CNT. Innovative use of camphor during sample synthesis enables precise control over the morphology of the filled CNT, which can either be in *aligned-forest* or in *entangled* geometry. The morphology appears to play a crucial role in tuning the *magnitude* of the specific capacity, whereas the *encapsulation* relates to the *cyclic stability*. Overall, the electrochemical data on various oxides@CNT bring forward interesting inferences pertaining to the morphology, filling fraction of the oxide-encapsulate, and the presence of oxide nano-particles adhering outside the CNT. Our results provide useful pointers for optimization of these critical parameters, thus paving the way for oxide@CNT for practical electrochemical applications.

---

[*] Author to whom any correspondence should be addressed.

1361-6463/23/425504+10$33.00 Printed in the UK

Supplementary material for this article is available online

Keywords: carbon nanotubes, transition metal oxides, Li Ion battery, anode materials

(Some figures may appear in colour only in the online journal)

## 1. Introduction

Hybrids based on carbon nanotubes (CNTs) and transition metal oxides (TMOs) are routinely explored in Li-ion batteries (LIBs) [1–22]. A primary advantage is the exceptional mechanical strength of the CNT, which can be utilized to buffer the volumetric strain during charging/discharging processes, associated with (bare) TMO based electrodes [2–4, 13–26]. This, coupled with the superior electrical conductivity of CNTs and the fact that the active material is secured within its core cavity should lead to better electrochemical performance. In spite of these advantages, applications based on such CNT/TMO hybrids are limited owing to practical limitations [27]. The endeavor of this work is to address some of these practical restrictions in utilization of such CNT hybrids in Li-ion batteries.

In order to do so, we first distinguish two distinct scenarios pertaining to the usage of CNT/TMO hybrids for LIBs in the literature. In the first case, the CNT and the TMOs are synthesized separately and pressed together to form the composite [16, 22, 23, 25, 26, 28–34]. In the second type, such hybrids are formed by synthetically encapsulating the oxide within the core cavity of the CNTs [2, 3, 17, 18, 20, 35]. In this work, we focus on *self-organized* CNT structures, belonging to the second case, with the TMOs synthetically encapsulated within the core cavity of the CNTs. These hybrids are referred to as oxides@CNT throughout the text. Actual encapsulation of the active material within the core cavity of CNT should, thus, circumvent the problem of capacity fading associated with volumetric strains, as opposed to that of oxide/CNT hybrids in which CNTs and TMOs are pressed together and hence oxide resides outside CNT. It is also to be noted that, while $FeO_x$@CNT has been tested as an anode material [2, 13, 20, 28, 33, 36], to the best of our knowledge $CoO_x$ & $NiO_x$@CNT with significant filling efficiencies (within the core cavity of the CNT) such as presented in this work have not yet been explored for LIBs. This is primarily due to difficulties related to the synthesis of NiO & $CoO_x$@CNT [37].

The paper is organized as follows. We first present a complete structural and electrochemical characterization of $Fe_3O_4$@CNT, $Co_3O_4$@CNT and NiO@CNT. Each sample is investigated to find correlations between the structural aspects and electrochemical properties. The effect of morphology is further explored with focus on just one sample, $Fe_2O_3$@CNT, formed in three distinct morphologies. These data reveal how the morphology of oxide@CNT and the residual oxide NP residing outside filled CNTs affect the cyclic stability and the magnitude of the capacity. Finally, we compare the cyclic stability of various oxides@CNT with that of a representative bare-oxide. Here, the bare-oxide has been derived from the corresponding oxide@CNT, and hence the bare-oxide retains the same morphology. This comparison enables us to isolate the advantages associated with the encapsulation of TMOs inside CNTs as compared to bare-oxides of similar shape and size. Synthesis protocol to form oxides@CNT is included in supplementary information (SI) Text S1. A more detailed account for the synthesis of oxides@CNT in the desired morphology can be found in [37].

## 2. Experimental details

The furnace employed for synthesis of the oxides filled CNTs was Nabertherm R 100/750/13. The scanning electron microscopy (FESEM) images were recorded using ZEISS ULTRA plus field-emission FESEM. This work centers around the correlation between the morphology of oxides@CNT and electrochemical data, additional broad-area SEM and TEM images have also been included as SI (figures S1–S3). All of the samples have been characterized using x-ray powder diffraction (XRD) using Bruker D8 Advance with Cu-K$\alpha$ radiation ($\lambda = 1.540\,56$ Å). The thermal analysis was determined by a thermogravimetric analyser, Perkin Elmer STA 6000, under air at 20 ml min$^{-1}$ at a heating rate of 15 °C min$^{-1}$ from 30 °C to 900 °C. Raman spectroscopy measurements were performed on HORIBA JOBIN YVON LabRam HR 800 with an excitation wavelength of 488 nm.

## 3. Results and discussions

### 3.1. Morphology of oxides@CNT: aligned-forest and entangled

We first present a schematic for defining the two types of morphology of oxides@CNT used in this work. The first is the *aligned-forest* depicted in figure 1(a). Here, the CNT network forms large *carpet-like* structures. The second is an *entangled* morphology as shown in figure 1(b), which consists of individually curled CNTs. Individual CNTs in both these morphologies are multiwalled and contain oxide-filling in the form of long and short nano-wires, as depicted schematically in figure 1(c). The oxide NPs can adhere outside the CNT (figure 1(c)) in both of these morphologies and the density of such NPs depends on the synthesis parameters [37, 38]. Oxides@CNT formed in *aligned-forest* morphology, such as shown in figure 1(a), lead to a narrow distribution of length and diameter of the individual CNT [37]. This factor can be favorable for the reproducibility of the electrochemical data. However, oxides@CNT in *entangled* morphology

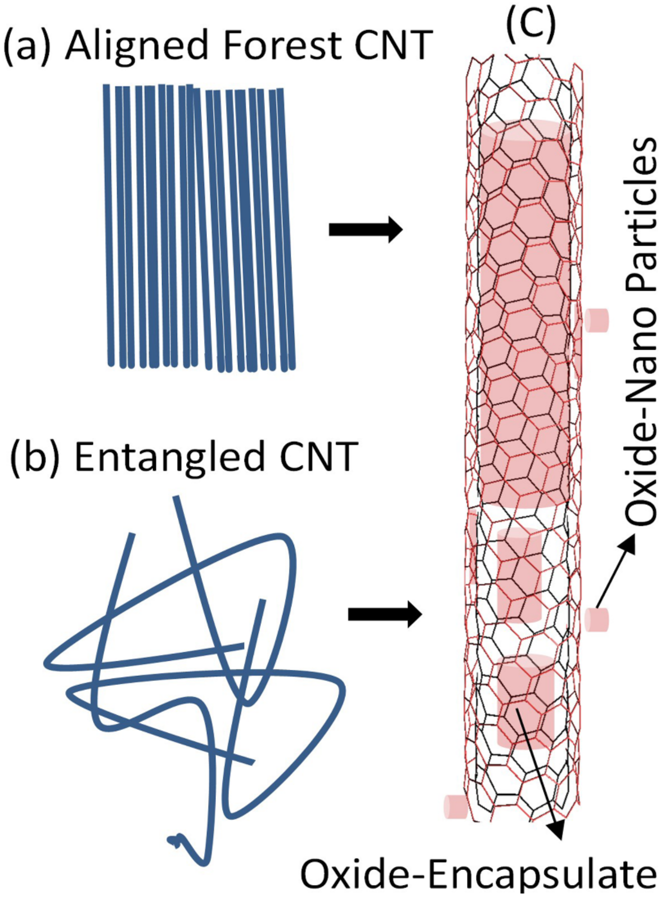

**Figure 1.** (a), (b) A schematic for *aligned-forest* and *entangled* morphologies for oxides@CNT. (c) The enlarged schematic of an individual (multi-walled) CNT, which encapsulates oxide in the form of long or short nano-wires within its core cavity. Residue oxide nano particles adhering outside the CNT shown in the schematic exist in both types of morphologies.

(figure 1(b)) are likely to be more conducive for Li-ion transportation during the electrochemical process, owing to the additional space available for the intercalation of Li ions. The morphology of the oxides@CNT also controls the conductance of the CNT network, and therefore relates to the overall performance of the cell, including capacity as well as the cyclic stability.

In this work, we investigate eight oxides@CNT samples, which contain four different types of oxide-encapsulate with different filling fractions, formed in either the *aligned-forest* or the *entangled* morphology and contain varying degrees of residual oxide nano-particles. The morphology and the residual nano-particle density in these samples can be controlled via synthesis parameters [37]. The mass corresponding to the *active-material* loading for each sample is the mass of the *as-prepared* oxide@CNT sample, which is inclusive of the CNT, the encapsulate as well as the residual oxide nano particles adhering outside the CNT. For synthetically encapsulated oxide@CNTs, such as discussed in this work, both the encapsulate and the residual nano-particles contribute to the active material, and hence, this total mass is relevant for practical applications. Correlations between the structural and electrochemical characterization can enable optimization of the best parameters for oxides@CNT systems for LIBs. These data are presented in the next sub-section.

### 3.2. $Fe_3O_4$@CNT, $Co_3O_4$ and NiO@CNT: structural characterization

Figures 2(a)–(c) shows the results of TGA measurements (main panel) along with broad area FESEM images (inset) for all three types of oxides@CNT. The oxide weight content was estimated to be 35% in the case of $Fe_3O_4$@CNT (red dots), 12% for NiO@CNT (green dots), and 54% in case of $Co_3O_4$@CNT (blue dots). The estimate for filling efficiencies and residual NP density can be further refined using FESEM and TEM images [37–39]. Broad area FESEM images, representative of ones shown in the inset of figures 2(a)–(c), reveal the overall morphology for each type of sample. Multiple FESEM and TEM images (supplementary figures S1–S3) not only confirm the presence of the encapsulate, but also provide a rough estimation of the residual NP density [37].

As evident from the FESEM images (figures 2(a)–(c)), $Fe_3O_4$@CNT and $Co_3O_4$@CNT are formed in carpet-like structures, with areas in the range of $\sim$ 100 square $\mu$m and thickness $\sim$ 20–30 $\mu$m. $Fe_3O_4$@CNT carpets consist of individual CNTs with *entangled* morphology, similar to what is shown schematically in figure 1(b). The length of an individual CNT in this case varies from 100 to 500 nm. The carpets in the case of $Co_3O_4$@CNT consist of *aligned-forest* morphology (figure 1(a)). The typical length and the outer diameter of the individual CNTs in this case are $\sim$ 20–30 $\mu$m and 20–40 nm respectively (figure 2(c)). We also note from FESEM and TEM images (supplementary figures S1–S3) that the number of oxide NPs adhering outside the CNT is slightly larger in the case of $Fe_3O_4$@CNT as compared to $Co_3O_4$@CNT. However, some large chunks of oxide are additionally observed to co-exist in the case of $Co_3O_4$@CNT (supplementary figure S3). The inset in figure 2(b) shows the FESEM image for NiO@CNT, depicting a granular morphology. The typical length of an individual CNT in this case ranges from 1 to 10 $\mu$m. The filling fraction as well as the residue particles adhering to the CNT are relatively less in NiO@CNT, as compared to $Fe_3O_4$@CNT. CNTs with well-formed graphitic shells are observed for all three samples, either in *aligned-forest* (insets of figure 2(c)) or in *entangled* morphology (figure 2(b)).

The samples were further characterized using XRD and Raman spectroscopy and a good match with the literature was observed. For instance, Raman peaks corresponding to the CNT were observed at $\sim$1356 cm$^{-1}$ (D band), $\sim$1578 cm$^{-1}$ (G band), and $\sim$2715 cm$^{-1}$ (2D or G' band) in case of $Fe_3O_4$@CNT as shown in figure 2(d). The D band is assigned to the disordered structures in the hexagonal sp$^2$ carbon network, and the G-band originates from the *in-plane* bond stretching motion of sp$^2$ carbon atoms [40]. The increase in the number of defects on the CNT surfaces may also have a contribution from strain associated with the oxide filling [41]. The contribution from $Fe_3O_4$ is also identified in Raman data [42]. The other two samples

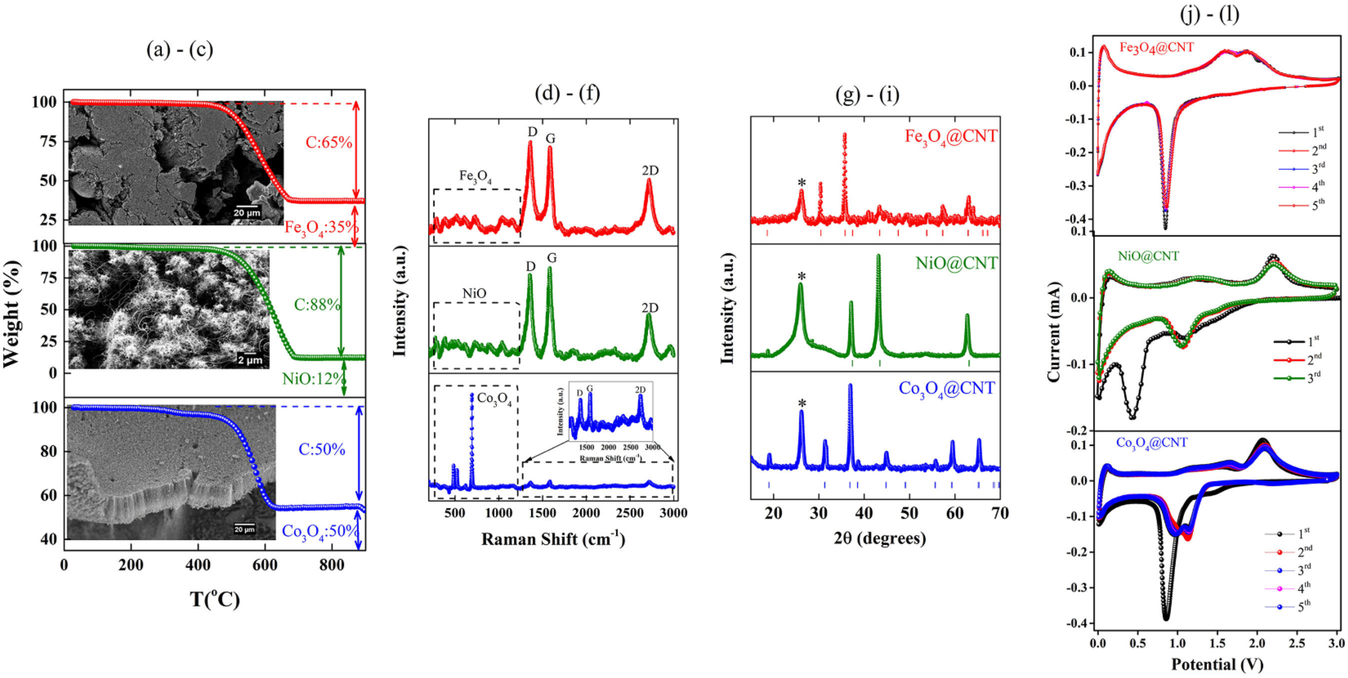

**Figure 2.** (a)–(c) TGA data for $Fe_3O_4$@CNT (red dots), NiO@CNT (green dots) and $Co_3O_4$@CNT (blue dots). The carbon and the oxide content as obtained from the TGA are indicated in (a)–(c). Broad area FESEM images in the respective insets reveal that $Fe_3O_4$@CNT as well as $Co_3O_4$@CNT are formed in the *aligned-forest* morphology and the NiO@CNT is formed in the *entangled* morphology. (d)–(f) Raman spectra depicting D, G, and 2D bands corresponding to CNTs. The characteristic peaks corresponding to the oxide encapsulate are also identified. (g)–(i) XRD data, with stars in each panel denoting the Bragg peak corresponding to the CNT, and the remaining peaks are identified with respective oxides. (j)–(l) Cyclic voltammetry (CV) curves of $Fe_3O_4$@CNT, NiO@CNT and $Co_3O_4$@CNT, between 3.0 and 0.1 V at a scan rate of 0.1 mV s$^{-1}$, characterizing oxide-metal conversion for each sample.

shown in figures 2(e) and (f) are also characterized along similar lines for identification of CNT and the respective oxide-encapsulate [43, 44]. Figures 2(g)–(i) show the XRD pattern of the oxides@CNT. The diffraction peak corresponding to CNT is observed at around 26.3° corresponding to the (002) plane (ICSD code: 015840), and the other peaks were identified as reflections from the corresponding oxides ($Fe_3O_4$ JCPDS No. 75-0033; NiO JCPDS No. 47-1049; $Co_3O_4$ JCPDS No. 42-1467).

### 3.3. $Fe_3O_4$@CNT, $Co_3O_4$ and NiO@CNT: electrochemical characterization

The reversibility and the kinetics of Li ion intercalation and de-intercalation for the oxides@CNT samples are studied using cyclic voltammetry (CV) measurements. The CV curves for the first three cycles are shown in figures 2(j)–(l) for all three oxides@CNT. In the first cycle shown in figure 2(j), a well-defined reduction peak at 0.85 V corresponds to the conversion of $Fe_2O_3$ into metallic Fe and the formation of SEI film [2, 20, 33]. The anodic peaks at 1.62 and 1.84 V represent the oxidation of Fe to $Fe_3O_4$. The anodic peaks show no significant difference in subsequent cycles, indicating reversibility and capacity stability. Similar data obtained on NiO@CNT and $Co_3O_4$@CNT shown in figures 2(k) and (l) are consistent with the previous reports on the electrochemical reaction of the respective bare oxides [18, 26]. The electrochemical reaction equation (supplementary text S2) and galvanostatic discharge/charge voltage profiles corresponding to each type of oxides@CNT are given as supplementary: figures S4(a)–(c).

Figures 3(a)–(c) show the discharge and charge profiles for all the three oxides@CNT, with active material loading $\sim 0.5\,\mathrm{mg\,cm^{-2}}$ for each sample. The cyclic stability of the sample $Fe_3O_4$@CNT shown in figure 3(a) at a current density of 200 mA g$^{-1}$ scanned for up to 100 cycles. The discharge capacity obtained in the first cycle is 950 mA h g$^{-1}$. This delivers a reversible capacity retaining a value of 570 mA h g$^{-1}$. The capacity is also observed to increase slightly during cycling. This tendency has been previously observed for metal oxide electrodes in long-term cycling [45]. Although no consensus has been reached in this regard, various possible reasons have been proposed, such as an increase in the surface area of the electrode due to pulverization, an increase in the conductivity owing to the formation of metallic nanoparticles, etc [45–51]. In our case, this feature appears to correlate with the *entangled* morphology of oxide@CNT, in addition to the increase in conductivity of the sample. As mentioned previously, the increase in the surface area and secondary voids present in *entangled* CNT can be a contributing factor for its better electrochemical performance. The issue is further elaborated and substantiated with more data in the latter part of the text. The specific capacity as a function of cycle number for the

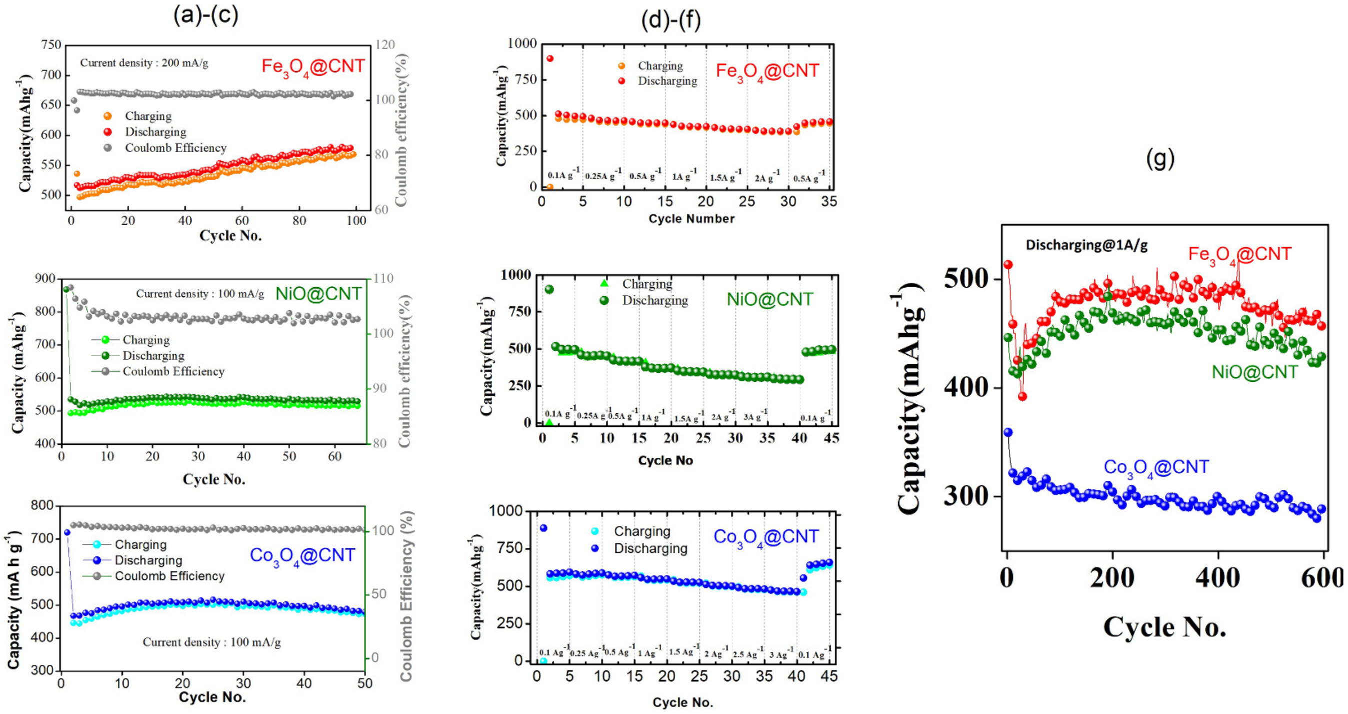

**Figure 3.** (a)–(c) Discharge and charge capacities and Coulomb efficiencies for $Fe_3O_4$@CNT (red dots), NiO@CNT (green dots) and $Co_3O_4$@CNT (blue dots), as a function of the cycle number. Discharge and charge capacity of Oxides@CNT at different current densities are shown in (d)–(f). (g) Specific capacity up as a function of cycle number (up to 600 cycles) for $Fe_3O_4$@CNT (red dots), NiO@CNT (green dots), and $Co_3O_4$@CNT(blue dots) at a current density of 1 A $g^{-1}$.

other two samples, NiO@CNT and $Co_3O_4$@CNT is shown in figures 3(b) and (c), respectively. Despite the differences in the filling fraction of the oxide and the over-all morphology, it is clear that oxides@CNT exhibit superior cyclic stability.

In addition to the cyclic stability, the high-rate proficiency of the electrode material is also an important factor for high power applications. The rate performance is shown in figures 3(d)–(f), and all samples were observed to deliver an outstanding rate performance even at high current densities. In case of $Fe_3O_4$@CNT, as the current densities are increased to 0.1, 0.25, 0.5, 1, 1.5, 2 A $g^{-1}$, the discharge capacities observed are 515, 472, 447, 425, 410, 390 mA h $g^{-1}$ respectively. When the current density is switched to 0.5 A $g^{-1}$, the capacity of $Fe_3O_4$@CNT is restored to a stable capacity of 540 mA h $g^{-1}$. A similar pattern is also observed for the other two samples as depicted in figures 3(e) and (f).

It is interesting to note that all the three oxides@CNT not only exhibit exceptional cyclic stability up to 100 cycles and for discharge rates of 100 mA $g^{-1}$ but also exhibit reasonable capacity, which is ∼ 500–600 mA h $g^{-1}$. Here, the magnitude of capacity is relatively higher for $Fe_3O_4$@CNT, which has a higher oxide content than NiO@CNT. However, $Fe_3O_4$@CNT forms in a carpet-like structure, which may be less conducive for Li-ion transportation, even though here the carpet consists of short (100–500 nm) and entangled CNTs. These filled and entangled CNTs, residing deep within this carpet, may not be as accessible as an active material, as opposed to, say, NiO@CNT, which has been formed in a proper *entangled* structure. Here, NiO@CNT consists of long (1–10 $\mu$m) and curled CNT, but the filling efficiency is poor in this case, as compared to $Fe_3O_4$@CNT. For the sample $Co_3O_4$@CNT, which has been formed in *aligned-forest* morphology, the filling efficiency is less and there is evidence of large chunks of oxide-particles residing outside the CNT. This is revealed from broad area FESEM images shown in supplementary figure S3. We conclude that despite the differences related to morphology, the cyclic stability is similar in all three oxides@CNT. Overall, these data suggest that superior cyclic stability is related to the encapsulation within the core cavity of the CNT and an optimal filling efficiency of 10%–20% leads to superior cyclic stability, which appears to be irrespective of the type of the oxide encapsulate.

The long term cycling performance of oxides@CNT was tested at a higher rate as shown in figure 3(g) up to 600 cycles. Here, the capacity for samples $Fe_3O_4$@CNT as well as NiO@CNT exhibit a slightly increasing trend up to 200 cycles. Beyond this, the reversible capacity stabilizes a value ∼ 450 mA h $g^{-1}$ up to 600 cycles. Both these samples contain CNTs with partial or proper *entangled* morphology and reasonable filling efficiency. On the contrary, $Co_3O_4$@CNT with *aligned-forest* morphology also exhibits good cyclic stability, but the magnitude of the capacity reduces when the cell is discharged at 1 A $g^{-1}$ for long-term cycling, as is evident from figure 4. This sample also contained large chunks of oxide NPs outside the CNT as is shown in supplementary figure S3. Thus,

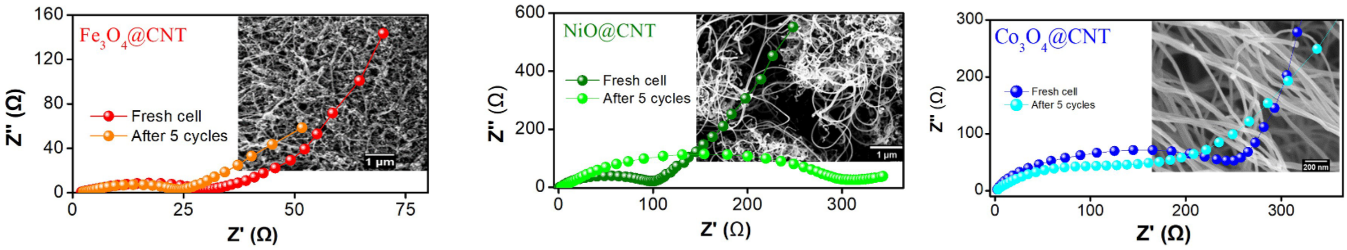

**Figure 4.** (a)–(c) Electrochemical impedance spectroscopy (EIS) spectra for fresh cells (black dots) and post five cycles (colored dots) for all three samples. The inset in each panel shows high magnification FESEM image of respective oxides@CNT.

it is clear that morphology and residue oxide NP contribute to the overall cell performance.

### 3.4. $Fe_3O_4$@CNT, $Co_3O_4$ and NiO@CNT: Nyquist plots

For further exploration of the correlation between morphology and the magnitude of the capacity, we performed electrochemical impedance spectroscopy (EIS) measurements for all three samples. The corresponding Nyquist plot obtained is shown in figures 4(a)–(c). On a general note, the large semicircle in the mid-frequency region of the Nyquist plot corresponds to the charge transfer resistance ($R_{ct}$), and the straight line in the low-frequency region characterizes the Warburg impedance of the Li-ion diffusion [23]. The region of the semicircle (corresponding to higher frequencies) in the Nyquist plot typically gives information about electrode resistance, reaction rate, double layer capacitance, etc, whereas the straight line (lower frequency region) reflects the diffusion coefficient of ions. Though a detailed analysis of the Nyquist plot for each oxide@CNT sample is beyond the scope of the present work, we focused on the semi-circular arc in the Nyquist plot for a comparative analysis of all three types of oxides@CNT. This region contains information about variations in the electrical resistance due to specific morphology and also to an extent depends on the electrode preparation details.

From figure 4(a) we note that the diameter of the semicircle in the mid-frequency region is significantly smaller than what has been observed in the previous reports on iron-oxide electrode materials [2, 20, 52]. The low Ohmic resistance signals easy electron transfer during the electrochemical Li ion insertion–extraction, resulting in an enhanced electrochemical performance of the electrode material. The $R_{ct}$ for $Fe_3O_4$@CNT is found to be $\sim 28\,\Omega$ as is evident from figure 3(g). The lower $R_{ct}$ is presumably due to an increased electrical conductivity facilitated by the well-connected CNT network in the carpet-like structure. Similar data on the other two oxides reveal that $R_{ct}$ for NiO@CNT and $CoO_x$@CNT is $\sim 100\,\Omega$ and $\sim 200\,\Omega$ respectively (figures 4(b) and (c)). We also note that $Fe_3O_4$@CNT and $Co_3O_4$@CNT exhibit similar values of $R_{ct}$ when a fresh cell is compared to the cell after five cycles. On the other hand, $R_{ct}$ for a fresh cell is significantly different from what is observed after five cycles in the case of NiO@CNT. The nature of the Nyquist plot in three different types of oxides@CNT, together with the structural and electrochemical characterizations presented in figures 2–4, provide a few pointers regarding the correlation between the two, as is highlighted in the next sub-section.

### 3.5. Oxides@CNT: correlations between structural and electrochemical data

From the FESEM images recorded at higher magnification in the inset of figures 4(a)–(c), we note that NiO@CNT and $Fe_3O_4$@CNT form in *entangled* morphology, but the CNT network connectivity is evidently better for $Fe_3O_4$@CNT which has a carpet-like structure (inset of figure 2(a)). On a similar note, the CNT network connectivity is also good for $Co_3O_4$@CNT. While an *aligned-forest* structure may be less conducive for Li-ion transport, the better CNT network connectivity of the electrode in this case is also likely to result in $R_{ct}$ after five cycles to be similar to that of the fresh cell. NiO@CNT exhibits long and curled CNTs with *entangled* morphology, but overall the CNT network is not uniform. It forms a rather granular structure, as is evident from the FESEM images shown in the inset and in supplementary figure S2.

Regarding the magnitude of capacity, we note that in the case of $Co_3O_4$@CNT, TGA data have shown 54% oxide content. However, multiple FESEM images reveal the presence of large chunks of isolated oxide particles in this sample (supplementary figure S3). This is in addition to the oxide NPs adhering outside the CNT. The filling efficiency in this case is certainly lower than $Fe_3O_4$@CNT. The large chunks of oxide particles adversely affect the overall battery performance in the case of $Co_3O_4$@CNT. Roughly the filling efficiency for all three samples is in the range of 10% to 25%, which appears to be related to good cyclic stability [37].

Electrochemical data on three different oxide@CNT with reasonable filling efficiency and widely different morphologies exhibit good cyclic stability. Some of the morphology related factors can have opposing contributions, as is also reflected from the corresponding Nyquist plots. It appears that these morphology-related effects average out, resulting in a similar magnitude of capacity for the three oxides@CNT, presented in figures 2 and 3. From the data obtained so far, it is evident that filling within the core cavity of CNT leads to superior cyclic stability. Moreover, it is also clear that factors, such as morphology and the presence of residual oxide NPs, appear to crucially influence the overall battery performance and need to be investigated systematically. We also

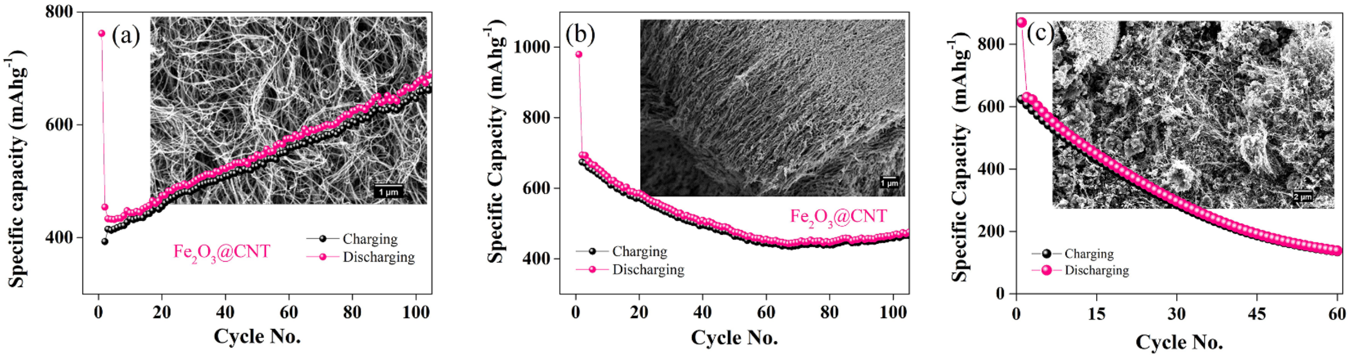

**Figure 5.** Effect of morphology and the residue particle density on the cyclic stability of (a) $Fe_2O_3$@CNT in *entangled* morphology (b) $Fe_2O_3$@CNT in *aligned-forests* morphology. The morphology of each type of $Fe_2O_3$@CNT sample is depicted in the respective FESEM images shown in the inset. (c) Cycling performance of sample $Fe_2O_3$@CNT with a large number of residue oxide nano-particles outside CNT conducted using a Swagelok-type cell. The morphology of the sample is depicted by the FESEM shown in the inset. The filling efficiency is also low in this case.

observed that electrode preparation details, including sonication of powders prior to cell fabrication, and connectivity of the CNT network appear to influence the battery performance. Here, we would like to emphasize that it is non-trivial to control morphology as well as the density of NPs adhering outside CNTs during synthesis. However, co-pyrolysis of camphor with metallocene during sample synthesis provided an additional parameter, which has enabled better control over these parameters [37]. With this approach, we could synthesize oxides@CNT with comparable filling efficiencies and NPs density but with different morphologies, especially in the case of $Fe_2O_3$@CNT.

To isolate the role of morphology, three samples of $Fe_2O_3$@CNT were investigated. Here, data are recorded for samples formed in *aligned-forest* and *entangled* morphologies, while keeping the filling efficiency in a similar range. These data are further compared with another sample of $Fe_2O_3$@CNT containing a large number of oxide NPs adhering outside the CNT, as discussed in the next sub-section.

### *3.6. $Fe_2O_3$@CNT: morphology of oxide@CNT and electrochemical data*

Figures 5(a)–(c) compare the cyclic performance of $Fe_2O_3$@CNT, in three different morphologies, with active material loading ∼0.5, 0.9, 1.9 mg cm$^{-2}$ respectively. FESEM images for these samples are shown in the respective inset. The samples with *entangled* and *aligned-forest* morphologies in figures 5(a) and (b) are tested for LIBs using a coin cell. In addition, another $Fe_2O_3$@CNT sample with a much larger fraction of residual NPs is also investigated in figure 5(c). The overall filling efficiency is lower in this case, as compared to the samples shown in figures 5(a) and (b). XRD data (not shown here) revealed that the sample also contains a tiny amount of $Fe_3O_4$.

It is interesting to note that the sample shown in figure 5(a) exhibits an increasing trend in the magnitude of specific capacity as a function of the cycle number. The FESEM image shown in figure 5(a) reveals that long and curled CNTs are uniformly formed in *entangled* morphology. As is evident from the main panel, an initial capacity of 400 mA h g$^{-1}$ increases up to 700 mA h g$^{-1}$ after 100 cycles. This type of trend has been observed earlier for $Fe_3O_4$@CNT in which individual CNTs are short and *entangled*, but they reside within a carpet-like structure figure 2(a)). However, it is evident that *entangled* morphology with a uniform texture in the case of $Fe_2O_3$@CNT leads to a much more pronounced increase in capacity. This increasing trend is expected to eventually stabilize on longer cycle runs, similar to what is shown in figure 3(g). However, these data suggest that properly formed *entangled* morphology appears to be conducive for achieving enhancement in the magnitude of the capacity. The *aligned-forest* structure, on the other hand, shows a slight reduction in capacity over cycle number, but eventually the capacity stabilizes, as is evident from figure 5(b). This sample contains a slightly larger number of residual NPs as compared to the one shown in figure 5(a) (supplementary figure S5). Thus, the results suggest that the *entangled* morphology with long and curled tubes, well-connected CNT networks and reasonable filling efficiency is more favorable for better cycle performance. The results of the $Fe_2O_3$@CNT sample (for which the Swagelok-type cell was used for characterization), with a large number of oxide NPs and with less filling efficiency, exhibit a much faster capacity fade as shown in the main panel of figure 5(c).

We also compared the same batch of $Fe_3O_4$@CNT samples, tested using a coin cell and a Swagelok-type cell. For both measurements, the $Fe_3O_4$@CNT powders were also sonicated prior to the electrode preparation. These results are shown in figure S6. Here, the magnitude of the capacity is about 450 mA h g$^{-1}$ with good cyclic stability observed in both cases. However, the minor differences can be attributed to electrode preparation details and the final texture of the pressed powders in both cases. Here, a slight difference can also arise due to the changes in conductance of the pressed powders.

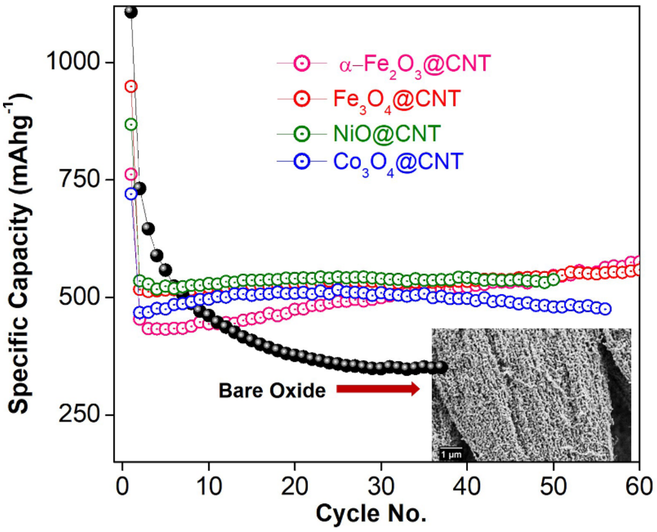

**Figure 6.** Oxides@CNT (coloured dots) deliver a stable discharge capacity, irrespective of the type of the oxide encapsulate, as compared to the bare oxide (black dots), which exhibits a decaying trend after the initial cycles. Here, the bare oxide is $Fe_2O_3$ in the form of *aligned-forests*, for which FESEM is shown in the lower inset.

Overall, we conclude that the encapsulation of oxide within the core cavity leads to better cyclic stability. The oxide NPs or isolated chunks of bare oxide may add to the magnitude of specific capacity but their presence is detrimental to cyclic stability, as is evident from figure 5. Thus, superior cyclic stability is primarily connected to encapsulation of oxide within the core cavity of the CNT.

### *3.7. Encapsulation and superior cyclic stability*

To confirm that superior cyclic stability in these Oxides@CNT nano-structures arises from encapsulation within the core cavity of the CNT, we conducted control measurements on the bare-oxide. Here, the representative bare-oxide ($\alpha$-$Fe_2O_3$) is formed in the same morphology as $Fe_2O_3$@CNT by suitable annealing [41]. The bare-oxide template was obtained from the same batch as $Fe_2O_3$@CNT, on which electrochemical measurements were performed. This enables us to check and isolate the effect of the morphology of the active material on the cyclic stability. These data, in conjunction with all oxides@CNT, are presented in figure 6. The morphology of the representative bare-oxide is shown in the inset of figure 6. The morphologies of the other oxides@CNT are shown in the inset of figures 2 and 5(a) and (b). Cyclic performance for all oxides@CNT shown in figure 6 are recorded at a current density of $100\,\mathrm{mA\,g^{-1}}$, except $Fe_3O_4$@CNT, which is recorded at $200\,\mathrm{mA\,g^{-1}}$. However, as is evident from figure 3(d), the magnitude of the capacity is similar for both current densities for $Fe_3O_4$. Data in figure 6 bring forward the superior cyclic stability for all of the oxides@CNT samples, irrespective of the type of oxide-encapsulate.

The black dots in figure 6 display the cycling performance of the bare oxide template, which is $Fe_2O_3$ at a current density of $100\,\mathrm{mA\,g^{-1}}$. The specific capacity of the bare oxide template drops down from $1100\,\mathrm{mA\,h\,g^{-1}}$ in the first cycle to $350\,\mathrm{mA\,h\,g^{-1}}$ after 35 cycles, thus, exhibiting a poor stability. The primary reason for the poor cyclic stability of the bare oxide materials in LIBs is known to arise from pulverization of the anode material. The drastic volume variations during metal-to-metal-oxide conversions lead to strain effects during the cyclic process, which together with low electrical conductivity in bare oxide leads to poor cycle life [27]. $Fe_2O_3$@CNT, on the other hand, exhibits superior cyclic stability (pink dots in figure 6) and cycle capacity retention. It is also evident that bare oxide ($\alpha$-$Fe_2O_3$ in this case) exhibits its poor cyclic stability as compared to not only $Fe_2O_3$@CNT but all other oxides@CNT, presented in figure 6. These oxides@CNT contain different types of oxide encapsulate with varying filling fractions and density of residue oxide NP. More importantly, data are available on oxides@CNT samples formed in different types of morphologies, such as *aligned-forests* or *entangled*. Nevertheless, all these oxides@CNT exhibit superior cyclic stability as compared to the bare-oxides. Thus, encapsulation of oxides within the core cavity of CNT accommodates strain related to metal to metal-oxide conversion [2].

We reiterate that all of the oxides@CNT presented in this work refer to CNT samples in which the oxide is synthetically encapsulated within its core cavity [37]. For filling efficiencies of the order of 10%–20% the magnitude of the capacity is almost similar for different oxide@CNT samples, however the cyclic stability significantly improves with encapsulation, as is evident from figure 6. Since oxide/CNT hybrids are extensively investigated for battery applications, we present a table to distinguish oxide/CNT hybrids in which oxide is synthetically encapsulated within the core cavity of CNT [2, 3, 17,

**Table 1.** Comparison of electrochemical performance of some Oxide & CNT hybrids including (i) synthetically encapsulated oxide within the core cavity of the CNT and (ii) Oxides/CNT hybrids, in which oxides and CNT are pressed together to form nano-composites.

| Sample | Type/morphology | Current density mA g$^{-1}$ | Discharge capacity [cycle no] mA h g$^{-1}$ | Reference |
|---|---|---|---|---|
| $Mn_3O_4$@CNT | Oxide@CNT | 100 | 461 [50] | [17] |
| $WS_2$/C | Composite | 100 | 525 [200] | [53] |
| $FeO_x$/CNT | Composite | 200 | 500 [50] | [36] |
| $FeO_x$@CNT | Oxide@CNT | 100 | 500 [50] | [2] |
| $FeO_x$@CNT | Oxide@CNT/ Entangled | 100 | 700 [100] | This work |
| $FeO_x$@CNT | Oxide@CNT/ Aligned-Forest | 200 | 500 [50] | This work |
| NiO/CNT | Composite/ Microspheres | 100 | 500 [50] | [26] |
| NiO@CNT | Oxide@CNT | — | — | — |
| NiO Nanoparticles | Microspheres | 100 | 122 [100] | [26] |
| NiO@CNT | Oxide@CNT/ Entangled | 100 | 540 [50] | This work |
| $CoO_x$/Graphene | Composite | 100 | 700 [25] | [18] |
| $CoO_x$@CNT | Oxide@CNT | — | — | — |
| $CoO_x$@CNT | Oxide@CNT | 100 | 475 [50] | This work |

18, 20], from the ones in which CNT and Oxides are synthesized separately and then pressed together [16, 22, 23, 25, 26, 28–34]. Table 1 shows a comparison of discharge capacities of various oxides containing both types of Oxide/CNT hybrids along with the bare oxides, in a similar range of current density.

## 4. Conclusions

We have conducted comprehensive electrochemical measurements on samples of CNT, in which four different types of TMOs have been encapsulated. Co-pyrolysis of metallocene with camphor has enabled oxide@CNT in two distinct morphologies, the *aligned-forest* and the *entangled*. Here, oxide@CNT is distinguished from CNT/TMO hybrids that are typically processed by mixing their individual constituents. Electrochemical data on different oxides@CNT formed with optimal filling efficiencies of the order of 10%–20% of the oxide-encapsulate within the core cavity of the CNT lead to much superior cyclic stability, as compared to the bare-oxide. Testing oxides@CNT with different morphologies but similar filling efficiencies further brings out the role played by oxide NPs adhering outside the CNT. The density of residual nano-particles residing outside the CNT may add to the magnitude of capacity, but their presence is detrimental to the cyclic stability. It is non-trivial to control residual NPs (or their agglomerates) which inevitably form during synthesis of oxide@CNT. However, multiple characterization techniques, particularly broad area scanning and transmission electron microscopy, together with TGA and XRD, enable us to isolate the contribution of these factors to the overall performance in LIB. The *entangled* morphology of the CNT network with reasonable filling efficiency and control of the residue oxide nano-particles during the synthesis of oxides@CNT leads to good cyclic stability as well as higher capacity. Overall, these data demonstrate that the magnitude of the capacity depends on the filling fraction, residue particle density as well as the morphology, whereas the cyclic stability stems from the encapsulation. This systematic study enables optimization of the best parameters and provides a roadmap for the usage of these synthetically encapsulated and self-organized oxides@CNT nano-structures for electrochemical applications.

## Data availability statement

All data that support the findings of this study are included within the article (and any supplementary files).

## Acknowledgment

The authors thank Mr J Parmar, Mr S C Purandare and Mr R Bapat (TIFR) for TEM measurements; Mr Anil Shetty (IISER-P) for SEM, Miss Edna Joseph (NCL, Pune) for TGA measurements. The authors also thank F Wilhelmi and L Deeg for experimental support. AB acknowledges DST, India for funding support through a Ramanujan Grant. S O and A B acknowledge DST Nano mission Thematic Unit Grant. ET, AO and RK acknowledge support by DFG via KL 1824/13-1.

## ORCID iD

Ashna Bajpai https://orcid.org/0000-0003-0807-2095

## References

[1] Wang Y, Zhuang Q, Li Y, Hu Y-L, Liu Y-Y, Zhang Q-B, Shi L, He C-X, Zheng X and Yu S-H 2022 *Nano Res.* **15** 5064

[2] Yan N, Zhou X, Li Y, Wang F, Zhong H, Wang H and Chen Q 2013 *Sci. Rep.* **3** 3392

[3] Thauer E *et al* 2020 *Molecules* **25** 1064

[4] Sun Q, ZCao Z J, Zhang J, Cheng H, Zhang J, Li Q, Ming H, Liu G and Ming J 2021 *Adv. Funct. Mater.* **31** 2009122

[5] Goyal A, Reddy A and Ajayan P 2011 *Small* **7** 1709

[6] Xu X, HTan Xi K, Xi K, Ding S, Yu D, Cheng S, Yang G, Peng X, Fakeeh A and Kumar R V 2015 *Carbon* **84** 491

[7] Wu Y, Wang J, Jiang K and Fan S 2014 *Front. Phys.* **9** 351

[8] Kurttepeli M, SDeng M F, Mattelaer F, Cott D J, Vereecken P, Dendooven J, Detavernier C and Bals S 2017 *ACS Appl. Mater. Interfaces* **9** 8055

[9] DiLeo R, Castiglia A, Ganter M J, Rogers R E, Cress C D, Raffaelle R P and Landi B J 2010 *ACS Nano* **4** 6121

[10] Nishidate K and Hasegawa M 2005 *Phys. Rev.* B **71** 245418

[11] Meunier V, Kephart J, Roland C and Bernholc J 2002 *Phys. Rev. Lett.* **88** 075506

[12] Salahdin O D *et al* 2022 *Appl. Phys.* A **128** 703

[13] Liu X, SLi A B, Akinwolemiwa B, Hu Di, Wu T and Peng C 2021 *Electrochim. Acta* **387** 138559

[14] Zhou H, Zhang L, Zhang D, Chen S, Coxon P R, He X, Coto M, Kim H K, Xi K and Ding S 2016 *Sci. Rep.* **6** 37752

[15] Zhang W-D, Xu B and Jiang L-C 2010 *J. Mater. Chem.* **20** 6383

[16] Cao Z and Wei B 2015 *Front. Mater.* **240**

[17] Ottmann A, Scholz M, Haft M, Thauer E, Schneider P, Gellesch M, Nowka C, Wurmehl S, Hampel S and Klingeler R 2017 *Sci. Rep.* **7** 13625

[18] Puthusseri D, Aravindan V, Madhavi S and Ogale S 2016 *Energy Technol.* **4** 816

[19] Tang X, Liang M, Zhang Y, Sun W and Wang Y 2019 *Dalton Trans.* **48** 4413

[20] Liu Y, Wu N, Wang Z, Cao H and Liu J 2017 *New J. Chem.* **41** 6241

[21] Ottmann A, Deeg L, Ghunaim R, Deeg L, Ghunaim R, Hampel S and Klingeler R 2020 *J. Alloys Compd.* **834** 155018

[22] Choi S H, Lee J H and Kang Y C 2015 *ACS Nano* **9** 10173

[23] Chen Y, Chen X and Zhang Y 2021 *Energy Fuels* **35** 6420

[24] SFang B D and Passerini S 2022 *Transition Metal Oxide Anodes for Electrochemical Energy Storage in Lithium- and Sodium-Ion Batteries* (Wiley) ch 4, p 55

[25] Ye H, Zheng G, Yang X, Zhang D, Zhang Y, Yan S, You L, Hou S and Huang Z 2021 *J. Electroanal. Chem.* **898** 115652

[26] Xu Y, Hou S, Yang G, Lu T and Pan L 2018 *J. Solid State Electrochem.* **22** 785

[27] Ji L, Lin Z, Alcoutlabi M and Zhang X 2011 *Energy Environ. Sci.* **4** 2682

[28] Jeong Y *et al* 2022 *J. Electroanal. Chem.* **904** 115905

[29] Bahadur A, Iqbal S and Shoaib M 2018 *Dalton Trans.* **47** 15031

[30] Song N J and Ma C 2018 *Int. J. Electrochem. Sci.* **13** 452

[31] Wang G, Meng Y, Wang L, Xia J, Zhu F and Zhang Y 2017 *Int. J. Electrochem. Sci.* **12** 2618

[32] Yang Z, Shen J and Archer L A 2011 *J. Mater. Chem.* **21** 11092

[33] Wang X, Liu X, Wang G, Xia Y and Wang H 2016 *Mater. Chem.* A **4** 18532

[34] Cao W, Hu A, Chen X, Liu X, Liu P, Tang Q and Zhao X S 2016 *Electrochim. Acta* **213** 75

[35] Wang K *et al* 2023 *J. Am. Chem. Soc.* **145** 12760

[36] Cheng J, Wang B, Park C-M, Wu Y, Huang H and Nie F 2013 *Chem. Eur. J.* **19** 9866

[37] Kapoor A, Singh N, Dey A B, Nigam A and Bajpai A 2018 *Carbon* **132** 733

[38] Dillon F, Bajpai A, Koos A, Downes S, Aslam Z and Grobert N 2012 *Carbon* **50** 3674

[39] Peci T and Baxendale M 2016 *Carbon* **98** 519

[40] Saito R, Dresselhaus G and Dresselhaus M S 1998 *Physical Properties of Carbon Nanotubes* (Imperial College Press)

[41] Kapoor A, Dey A B Garg C and Bajpai A 2019 *Nanotechnology* **30** 385706

[42] de Faria D L A, Silva S V and de Oliveira M T 1997 *Raman Spectrosc.* **28** 873

[43] Mironova-Ulmane N, Kuzmin A and Sildos I 2011 *Cent. Eur. J. Phys.* **9** 1096

[44] Hadjiev V, Iliev M and Vergilov I 1988 *J. Phys. C: Solid State Phys.* **21** 199

[45] Luo J, Liu J, Zeng Z, Ng C F, Ma L, Zhang H, Lin J, Shen Z and Fan H J 2013 *Nano Lett.* **13** 6136

[46] Laruelle S, Grugeon S, Poizot P, Dollé M, Dupont L and Tarascon J-M 2002 *J. Electrochem. Soc.* **149** A627

[47] Tang J, Lugo C, Guzmàn S, Daniel G, Kessler V G, Seisenbaeva G A and Pol V G 2016 *J. Mater. Chem.* A **4** 18107

[48] Wang Z, Luan D, Madhavi S, Hu Y and Lou X W (D) 2012 *Energy Environ. Sci.* **5** 5252

[49] Jiang Y, Jiang Z, Yang L, Cheng S and Liu M 2015 *J. Mater. Chem.* A **3** 11847

[50] Zhou G, Wang D, Li F, Zhang L, Li N, Wu Z-S, Wen L, Lu G Q (M) and Cheng H-M 2010 *Chem. Mater.* **22** 5306

[51] Huang X, Chen J, Lu Z, Yu H, Yan Q and Hng H H 2013 *Sci. Rep.* **3** 2317

[52] Huang Y *et al* 2017 *Nano Energy* **41** 426

[53] Guo P, Singer L, Zhao Z, Kukułka W, Sebastian F, Mijowska E, Zharnikov M, Comba P and Klingeler R 2023 *Electrochim. Acta* **459** 142540